

RESEARCH ARTICLE | *Imaging Techniques in Renal (patho)Physiology Research*

# In vivo three-dimensional photoacoustic imaging of the renal vasculature in preclinical rodent models

Olumide Ogunlade,<sup>1\*</sup> John J. Connell,<sup>2\*</sup> Jennifer L. Huang,<sup>3</sup> Edward Zhang,<sup>1</sup> Mark F. Lythgoe,<sup>2</sup> David A. Long,<sup>3</sup> and Paul Beard<sup>1</sup>

<sup>1</sup>Department of Medical Physics and Biomedical Engineering, University College London, London, United Kingdom; <sup>2</sup>Centre for Advanced Biomedical Imaging, Division of Medicine, University College London, London, United Kingdom; and

<sup>3</sup>Developmental Biology and Cancer Programme, Great Ormond Street Institute of Child Health, University College London, London, United Kingdom

Submitted 30 June 2017; accepted in final form 11 December 2017

**Ogunlade O, Connell JJ, Huang JL, Zhang E, Lythgoe MF, Long DA, Beard P.** In vivo three-dimensional photoacoustic imaging of the renal vasculature in preclinical rodent models. *Am J Physiol Renal Physiol* 314: F1145–F1153, 2018. First published December 20, 2017; doi:10.1152/ajprenal.00337.2017.—Noninvasive imaging of the kidney vasculature in preclinical murine models is important for the assessment of renal development, studying diseases and evaluating new therapies but is challenging to achieve using existing imaging modalities. Photoacoustic imaging is a promising new technique that is particularly well suited to visualizing the vasculature and could provide an alternative to existing preclinical imaging methods for studying renal vascular anatomy and function. To investigate this, an all-optical Fabry-Perot-based photoacoustic scanner was used to image the abdominal region of mice. High-resolution three-dimensional, noninvasive, label-free photoacoustic images of the mouse kidney and renal vasculature were acquired in vivo. The scanner was also used to visualize and quantify differences in the vascular architecture of the kidney in vivo due to polycystic kidney disease. This study suggests that photoacoustic imaging could be utilized as a novel preclinical imaging tool for studying the biology of renal disease.

photoacoustic imaging; renal vasculature; polycystic kidney disease

## INTRODUCTION

The kidney is a highly vascular organ that receives over 10% of the cardiac output. Within the kidney there is a vast microvasculature consisting of the glomerular capillary network, peritubular capillaries, and vasa rectae, which are critical for blood filtration and electrolyte control. The vasculature plays a critical role in the progression of chronic kidney disease (CKD). Regardless of the initial insult, CKD progression is associated with remodelling of the renal vasculature eventually leading to capillary loss in the kidney (21). The association of the renal vasculature with CKD has led to numerous preclinical studies using vascular growth factors (6, 8, 12) or endothelial progenitor cells (22, 34) to attempt to revascularize the kidney as a means to restoring renal function.

To date, the majority of studies have utilized histological techniques to visualize the renal vasculature. However, new

insights into disease progression and therapeutic response may now be possible through the use of in vivo imaging techniques, which can provide serial longitudinal three-dimensional (3D) information about the vasculature. Magnetic resonance imaging (MRI) (14), ultrasound (19), and high-resolution micro X-ray computed tomography (micro-CT) (10) have been used to study renal structure and function in mice. However, with these imaging modalities, the relatively low intrinsic contrast from the microvasculature often necessitates the use of exogenous contrast agents introducing additional procedural complexity. In addition, high-resolution micro-CT (24) requires high X-ray doses limiting the number of repeat measurements in longitudinal studies.

Photoacoustic imaging (PAI) is an emerging noninvasive technique that offers the prospect of overcoming these limitations (1). It relies on the generation of ultrasound waves through the absorption of short, low-energy nonionizing laser pulses by light absorbing molecules, such as hemoglobin. By detecting the time-of-arrival of these waves at the tissue surface, an absorption-based image of the internal tissue structure can be reconstructed. The fundamental advantage of PAI is that optical contrast is encoded on to acoustic waves, which are scattered much less than photons. As a consequence, it avoids the depth and spatial resolution limitations of purely optical imaging techniques that arise due to strong light scattering in tissue: with PAI, depths of a few centimeters with scalable spatial resolution ranging from tens to hundreds of micrometers (depending on depth) are achievable. PAI contrast is defined largely by optical absorption. This makes it particularly well suited to visualizing the vasculature without the use of contrast agents due to the strong absorption of hemoglobin at visible and near infrared wavelengths (1, 18). Unlike existing imaging modalities it also offers the prospect of acquiring functional information via the measurement of both blood oxygen saturation (7) and flow (4).

Several preliminary PAI studies have been undertaken in which the structure of murine kidneys has been visualized by exploiting endogenous hemoglobin contrast (3, 15, 25). In addition, by introducing exogenous contrast, renal perfusion has been imaged in vivo using PAI (5, 23). In all of these studies, however, conventional piezoelectric-based photoacoustic scanners were used, which provided insufficient image quality to clearly visualize the kidney vasculature and differ-

\* O. Ogunlade and J. J. Connell contributed equally to this work.

Address for reprint requests and other correspondence: O. Ogunlade, Univ. College London, UCL, Gower St., London WC1E 6BT, UK (e-mail: o.ogunlade@ucl.ac.uk).

entiate it from other structures in either healthy kidneys or those with disease-mediated vascular abnormalities (20).

This current study extends previous work in terms of both methodology and application. Here we apply a new type of photoacoustic (PA) scanner based on an entirely different detection technology (i.e., all-optical) to previous scanners for studying the kidney in mice. This enabled the acquisition of significantly more detailed noninvasive 3D PA images of the mouse kidney and renal vasculature than previous PAI studies. Furthermore, we exploit this enhanced imaging performance to demonstrate the feasibility of PAI as a tool for studying renal disease by acquiring the first in vivo images of the abnormal renal vasculature in a preclinical murine model of polycystic kidney disease (PKD).

## MATERIALS AND METHODS

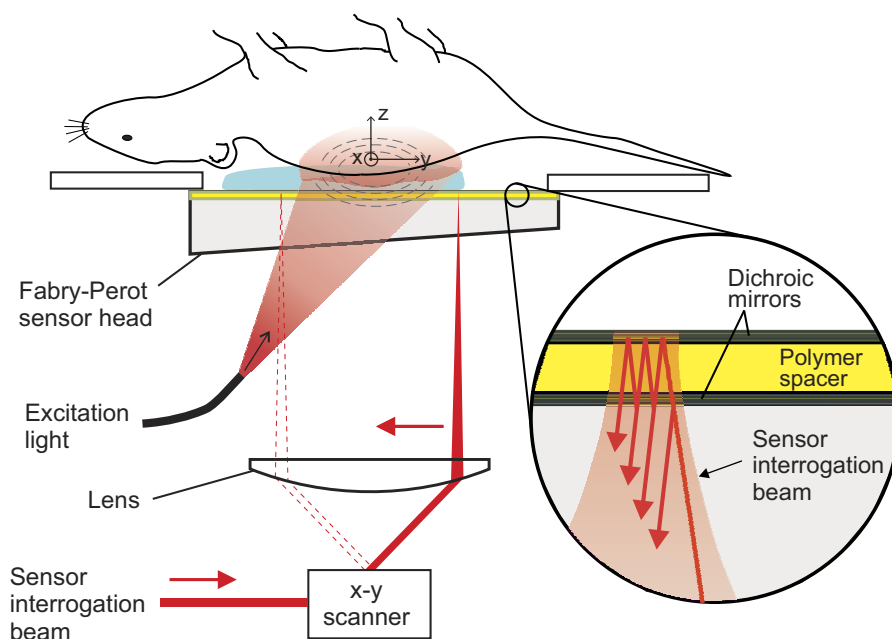
**Photoacoustic imaging.** PA signals were acquired using a high-resolution, all-optical, planar PA scanner based on a Fabry-Perot (FP) polymer film ultrasound sensor (13, 17, 35). A schematic of the scanner is shown in Fig. 1. Briefly, it consists of a fiber-coupled, tunable optical parametric oscillator laser system (Quanta Ray Pro-270/premiScan; Newport Spectra Physics/GWU Lasertechnik), which generates 7-ns excitation light pulses at a pulse repetition frequency of 50 Hz. The sensor is a thin film structure consisting of two dichroic mirrors separated by a 22- $\mu\text{m}$ -thick polymer spacer thus forming a FP etalon. The mirrors are designed to be transparent in the wavelength range from 590 to 1,200 nm but highly reflective between 1,500 and 1,600 nm. The transparency of the sensor in the former wavelength range means that the excitation light (wavelengths in the range 640–850 nm were used in this study) can be transmitted through the sensor into the adjacent tissue. The absorption of the light by the tissue generates PA waves that propagate back to the FP sensor, where they modulate the optical thickness of the polymer spacer. This produces a corresponding change in the reflectivity of the sensor, which is read out by scanning a 1,550-nm focused interrogation laser beam over its surface using a galvanometer-based  $x$ - $y$  scanner. The resulting time-varying modulation of the reflected interrogation beam, representing the PA signal, is detected by a photodiode and recorded by a digitizer. The sensor has a broadband frequency response with a  $-3$ -dB

bandwidth of 39 MHz, and the optically defined element diameter was 22  $\mu\text{m}$  (35). This combination of broad detection bandwidth and very small optically defined element size provides a performance advantage over conventional piezoelectric detector-based PA scanners, resulting in improved image quality. The scanner provides a maximum lateral field of view of  $20 \times 20$  mm and a penetration depth of  $\sim 10$  mm depending on excitation wavelength (13, 17, 35).

For in vivo imaging, where required, the fur of the mouse around the abdomen was removed with depilatory cream before the animal was placed on the scanner. Acoustic coupling was achieved between the sensor and the mouse by inserting a small amount of ultrasound coupling gel. The mouse was anaesthetized using isoflurane in oxygen [4% (vol/vol) at a flow rate of 2 l/min for induction and 1.5% (vol/vol) at a flow rate of 1 l/min for maintenance]. An integrated heater and thermal chamber, set to  $34^\circ\text{C}$ , was used to prevent hypothermia of the anaesthetized mouse (31). Ex vivo imaging of the kidneys in situ was achieved by submerging a mouse, culled with an overdose of sodium pentobarbital, in a sensor tank containing water or 0.2% intralipid, the latter to homogenize the incident light. For ex vivo imaging of excised kidneys, the renal artery and vein were cauterized immediately after excision. The kidneys were then placed in direct contact with the sensor and submerged either in water or a 0.2% intralipid suspension. To obtain the best compromise between contrast and penetration depth, images were typically acquired at multiple wavelengths in the range 620–920 nm. The maximum pulse energy used at these wavelengths was 18 mJ. The beam diameter was 2 cm; thus the maximum fluence at the surface of the skin was  $5.7 \text{ mJ/cm}^2$ . The imaged area was typically  $14 \times 14$  mm in steps of 100  $\mu\text{m}$ . For each scan,  $\sim 20,000$  waveforms, each containing 600 time samples with a temporal sampling interval of 20 ns, were acquired without signal averaging or respiratory gating, in  $\sim 7$  min. All in vivo animal experiments were approved by a local ethical review panel at University College London and were performed in accordance with the UK Home Office Animals Scientific Procedures Act (1986).

3D PA images were reconstructed from the acquired waveforms, using a time reversal algorithm (29) with a correction for acoustic attenuation in tissue implemented using a time-variant filtering method (26). The time reversal algorithm was implemented using k-Wave, an open source MATLAB toolbox developed at University College London for the time-domain simulation and reconstruction of PA and ultrasound wave fields (www.k-wave.org; Ref. 27). Before

Fig. 1. Schematic illustrating the Fabry-Perot-based photoacoustic scanner, showing a mouse placed in supine position for imaging. Photoacoustic signals, generated from the absorption of pulsed excitation light by tissue, are detected by the Fabry-Perot polymer film ultrasound sensor. *Inset:* an expanded view of the sensor. It comprises a polymer spacer sandwiched between a pair of dichroic mirrors that are transparent to the excitation laser wavelength but highly reflective to the sensor interrogation beam wavelength. The sensor operates by raster scanning a focused continuous wave interrogation laser beam across it and measuring the change in the power of the reflected beam produced by acoustically induced changes in the spacer thickness.



reconstruction, the raw PA signals were interpolated onto a three times finer  $x$ - $y$  grid. The sound speed used in the reconstruction was selected using an autofocus approach, based on a metric of image sharpness (28). An exponential function normalization with respect to depth was applied to the reconstructed image data set as a first-order correction for the effect of optical attenuation to aid visualization. Each 3D volume-rendered image required one reconstructed data set. The voxel size in the rendered volume was  $33.3 \times 33.3 \times 30.8 \mu\text{m}$ , determined by the spatial sampling in the reconstructed data. Where the reconstructed images were displayed as maximum intensity projections (MIPs), a logarithmic image intensity scale was used. Manual segmentation, false coloring, 3D volume rendering, and extracting a skeleton of the vasculature were implemented using Amira (FEI Visualization Sciences).

**Mouse models.** Twelve-week-old BALB/c mice were used to perform PAI of healthy kidneys. In addition, *Pkd1<sup>nl/wt</sup>* heterozygous mice (16), maintained on a CD1 background were bred to generate *Pkd1<sup>wt/wt</sup>* (wild-type) and *Pkd1<sup>nl/nl</sup>* (PKD) mice. Wild-type and PKD mice ( $n = 2$  and  $3$  respectively) were imaged in vivo at 8 days after birth or at 12 wk of age ( $n = 1$ ), with one kidney embedded in agarose after excision and used for MRI imaging and the other for PAI.

**MRI.** Ex vivo kidney specimens were embedded in 1% (wt/vol) agar gel and positioned in a 35-mm Rapid radiofrequency coil within a 9.4T Agilent preclinical MRI scanner. T2-weighted images were acquired using a multislice fast spin-echo sequence (repetition time of 1 s, echo time of 20 ms, ten 1-mm-thick slices, 4 averages, and data matrix  $256 \times 256$ ). The image acquisition time was 4 min for a field of view of  $30 \times 30 \text{ mm}^2$ , with in plane resolution of  $\sim 120 \mu\text{m}$ .

## RESULTS

In the first instance, preliminary exploratory studies were undertaken on a culled 12-wk old BALB/c mouse to optimize the light delivery and the positioning of the mouse to achieve the best visualization of the kidneys. The mouse was orientated in a supine position on the scanner and the abdomen illuminated (Fig. 1). 3D image data sets of the same mouse in two different positions were acquired. Horizontal ( $x$ - $y$ ) and vertical ( $x$ - $z$ ) MIPs of the 3D image data set acquired for one position of the mouse are shown in Fig. 2, *A* and *B*, respectively. These images show several organs and anatomical structures within the abdominal cavity. The two kidneys (*k*) located on either side of the spine (*s*) can be seen in both the  $x$ - $y$  and  $x$ - $z$  MIPs, with their location relative to the spine most apparent in the  $x$ - $z$  MIP (Fig. 2*B*). In Fig. 2*A*, the left-hand kidney is most clearly visible revealing the larger vessels of the renal vascular tree set against an oval-shaped region (indicated by the yellow arrows) of near uniform contrast originating from the kidney capillary bed. Part of the spleen (*sp*) is also visible in the horizontal MIP (Fig. 2*A*). Figure 2*C* shows a volume-rendered image from the same data set in which the kidneys were manually segmented and false colored. This image is shown as a horizontal projection in the same plane as the  $x$ - $y$  MIP in Fig. 2*A* but viewed from the underside. This enables the kidneys and the branched renal blood vessels to be visualised more clearly than the MIP; these blood vessels are even more apparent in the animated 3D representation of Fig. 2*C* available online (Supplemental Movie S1; Supplemental Material for this article is available online at the Journal website). The mouse was then repositioned to provide an alternative view so that the whole of the spleen, only a small portion of which was visible in the previous position, was located in the field of view. The corresponding horizontal ( $x$ - $y$ ) and vertical ( $x$ - $z$ ) MIPs acquired with the mouse in this position are shown in Fig. 2, *D* and *E*,

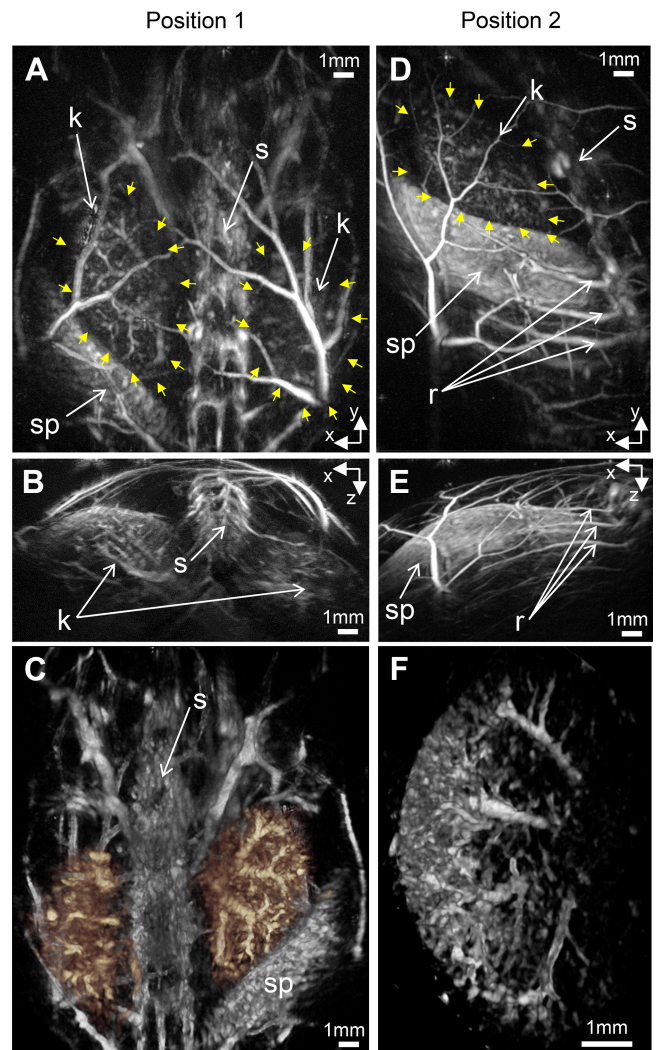
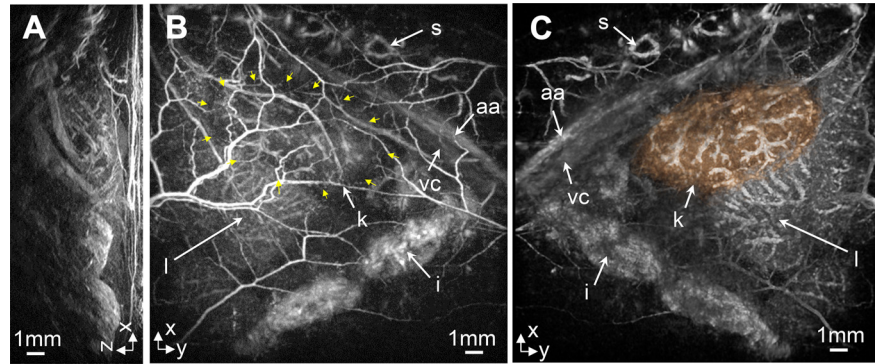


Fig. 2. In situ photoacoustic (PA) images of the abdominal cavity of a 12-wk-old BALB/c mouse, in 2 different positions, acquired at an excitation wavelength of 758 nm. **Position 1:** (*A*):  $x$ - $y$  maximum intensity projection (MIP); the spine (*s*) can be seen in the center of the image and the kidneys (*k*, outlined with yellow arrows) can be seen either side of the spine. Part of the spleen (*sp*) is also visible. (*B*):  $x$ - $z$  MIP also showing the kidneys (*k*) and spine (*s*). (*C*): 3D volume-rendered image of the same data set viewed from the underside to better visualise the kidneys and the renal vasculature; the kidneys are manually segmented and false colored, revealing blood vessels which are not apparent in the MIPs. An animated representation of this image can be viewed online at Supplemental Movie S1. **Position 2:** (*D*):  $x$ - $y$  MIP and (*E*):  $x$ - $z$  MIP. As well as the kidney (*k*, outlined with yellow arrows) and the spine (*s*), the whole of the spleen (*sp*) is now seen prominently, alongside ribs (*r*) attached to the spine. (*F*): 3D volume rendering of the kidney manually segmented from the data set shown in *D* and *E*, showing the vascular tree of the kidney. An animated representation of this image can be viewed online at Supplemental Movie S2.

respectively. As well as the kidney and spleen, several ribs (*r*) connected to the spine are also visible. The 3D image data set was manually segmented and volume rendered to visualize only the kidney as shown in Fig. 2*F*. Similar to Fig. 2*C*, the volume-rendered image allows visualization of blood vessels not readily apparent in the MIPs. Again, this is most clearly apparent in the animated representation of Fig. 2*F* (Supplemental Movie S2). Profiles were also taken across small blood vessels in the data set shown in Fig. 2, *A*-*C*. The full-width

Fig. 3. In vivo PA imaging of a 12-wk-old BALB/c mouse kidney.  $x$ - $z$  MIP (A),  $x$ - $y$  MIP (B), and volume-rendered image (C) of a 3D data set acquired at an excitation wavelength of 850 nm. The volume rendered image (C), viewed from the underside, reveals renal vasculature which is partially obscured by the brighter intensity of superficial anatomy in the MIP (B). In addition to a kidney (k, outlined with yellow arrows in B), the inferior vena cava (vc) and the abdominal aorta (aa) branching into the renal vein and artery can be seen. The spine (s) and one lobe of the liver (l), and part of the intestines (i) can also be seen. In C, the kidney is manually segmented and false colored. An animated representation of the 3D volume-rendered image can be viewed online at Supplemental Movie S3.



half-maximum of a Gaussian fit to these profiles provides an estimate of the spatial resolution of the scanner. The depth-dependent spatial resolutions obtained were as follows: 59  $\mu$ m at 600  $\mu$ m, 75  $\mu$ m at 1.5 mm, 113  $\mu$ m at 3.4 mm, 128  $\mu$ m at 5 mm, and 158  $\mu$ m at 7 mm.

After the optimum orientation of the mouse was established as described above, in vivo images of the kidney of an anaesthetized mouse were acquired. These are shown in Fig. 3, A and B, as  $x$ - $z$  and  $x$ - $y$  MIPs, respectively, as well as a volume-rendered 3D image in Fig. 3C in which the kidney is false colored. The kidney (k) and its vasculature can be seen in Fig. 3, B and C, as well as the abdominal aorta (aa) and inferior vena cava (vc), which branch into the renal artery and vein feeding the kidney. The branching is most clearly apparent in

the animated movie of Fig. 3C available online (Supplemental Movie S3). Collectively, the data in Figs. 2 and 3 illustrate the high level of detail with which the renal vessels can be visualized using the FP scanner. This suggests the system could be useful for studying kidney diseases characterized by changes in the renal vasculature.

To explore this possibility, we imaged 12-wk-old *Pkd1*<sup>nl/nl</sup> mice, which carry two hypomorphic alleles of *Pkd1*, the mouse homolog of the gene most commonly mutated in human autosomal dominant PKD, and their wild-type littermates (*Pkd1*<sup>wt/wt</sup>) (16). In the first instance, excised kidneys from *Pkd1*<sup>nl/nl</sup> and *Pkd1*<sup>wt/wt</sup> mice were studied. From visual inspection, the excised kidneys from the *Pkd1*<sup>nl/nl</sup> mice are evidently larger than those from *Pkd1*<sup>wt/wt</sup> with a paler looking appear-

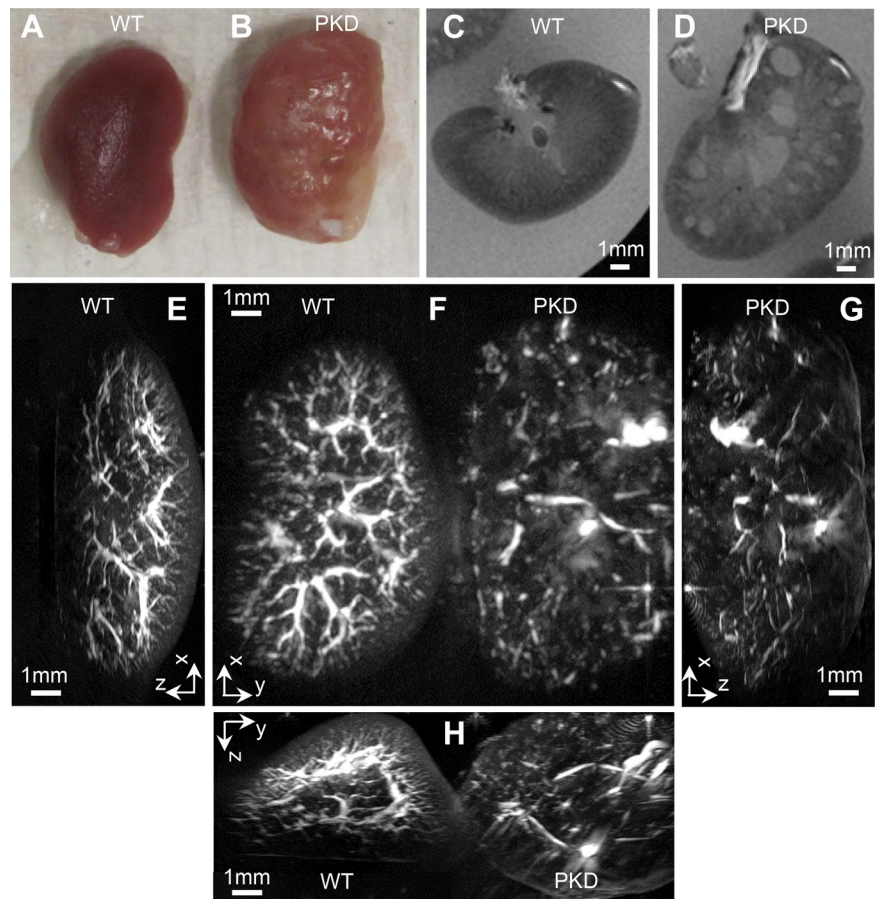


Fig. 4. Ex vivo imaging of excised kidneys: photograph, T2-weighted MRI, and PA images of mouse model of PKD (*Pkd1*<sup>nl/nl</sup>) and wild-type (WT) littermates (*Pkd1*<sup>wt/wt</sup>) showing structural differences. Photograph of kidneys from *Pkd1*<sup>wt/wt</sup> (A) and *Pkd1*<sup>nl/nl</sup> (B). The PKD kidney has a paler color and appears larger than the wild-type. T2-weighted MRI images of *Pkd1*<sup>wt/wt</sup> (C) and *Pkd1*<sup>nl/nl</sup> (D) kidney embedded in agarose, revealing the presence of fluid filled cysts in the PKD model. PA MIPs,  $x$ - $z$  (E and G),  $x$ - $y$  (F), and  $y$ - $z$  (H), of a 3D image data set of PKD and wild-type (WT) control kidneys, acquired using 640 and 795 nm excitation wavelengths simultaneously. Note the sparse and disorganised vasculature of the PKD kidney compared with that of the normal (WT) kidney. The PA images are of the photographed kidneys while the MRI images are of the contralateral kidney from each mouse. An animated representation of 3D volume-rendered PA images of the wild-type (Supplemental Movie S4) and PKD kidney (Supplemental Movie S5) can be viewed online.

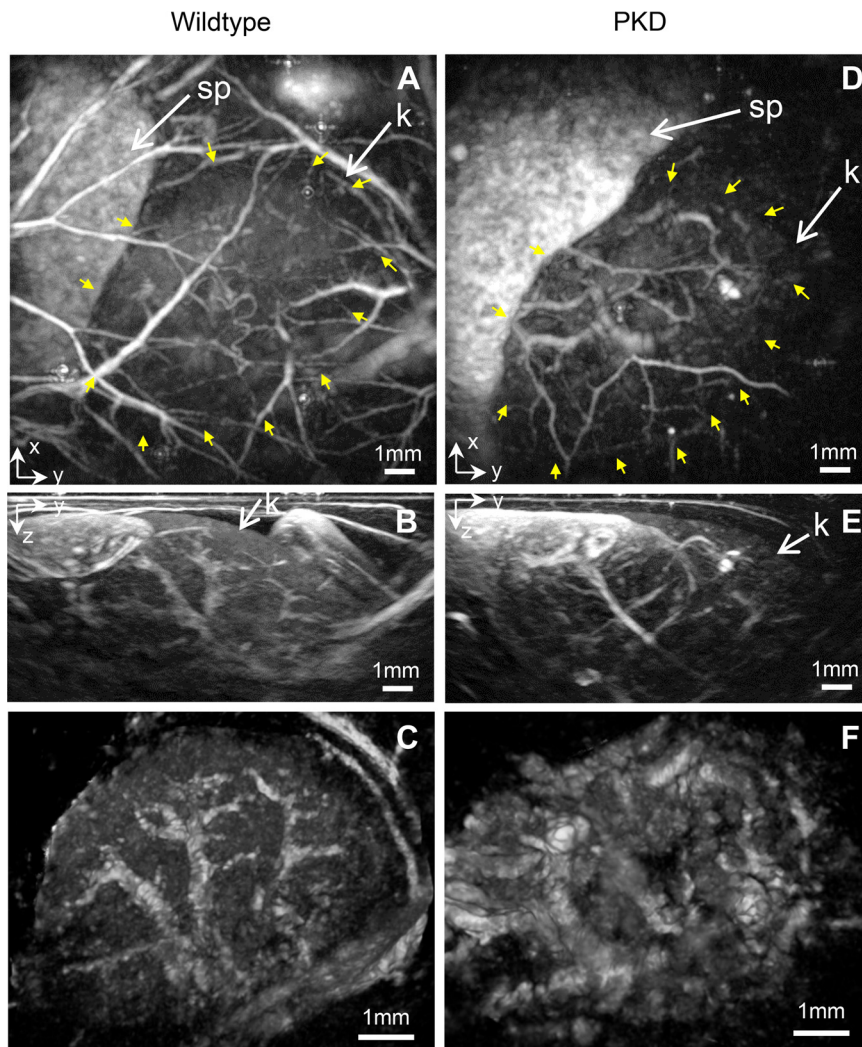


Fig. 5. In vivo PA images of mouse model of a 12-wk-old wild-type (A–C) and polycystic kidney (D–F). A and D:  $x$ - $y$  MIPs. B and E:  $y$ - $z$  MIPs. C and F: 3D volume rendering of the kidneys manually segmented from the data set shown in the MIPs above. These images were acquired at 800 nm. In the  $x$ - $y$  MIPs, the region where the kidneys are located is indicated by the yellow arrows. The  $y$ - $z$  MIPs and volume-rendered images, show that the ordered branching of the vessels in the wild-type kidney is replaced by a chaotic network of vessels in the polycystic kidney model. Animated representations of the volume-rendered images in C and F can be viewed online at Supplemental Movies S6 and S7; these animated representations show the differences in the vascular architectures of the wild-type and polycystic kidneys most clearly.

ance (Fig. 4, A and B). MR images (Fig. 4, C and D) revealed the presence of cysts in the *Pkd1<sup>nl/nl</sup>* mice, which were absent in *Pkd1<sup>wt/wt</sup>* animals. The kidney vasculature is however not visible in the MR image of either the PKD or wild-type kidney. On the other hand, the PA images (Figs. 4, E–H, and Supplemental Movies S4 and S5) show striking differences in the kidney vasculature with a marked decrease in overall vessel density in *Pkd1<sup>nl/nl</sup>* compared with *Pkd1<sup>wt/wt</sup>* mice. In addition, the ordered branching of the vessel tree seen in the wild-type kidney is not replicated in the PKD model, which shows a vascular architecture that is disorganized and sparsely distributed.

Having demonstrated that PAI can distinguish between the normal and diseased renal vasculature in an excised kidney, PA images were subsequently acquired in vivo in 12-wk-old *Pkd1<sup>wt/wt</sup>* (Fig. 5, A–C) and *Pkd1<sup>nl/nl</sup>* mice (Fig. 5, D–F). The images are shown as  $x$ - $y$  MIPs (Fig. 5, A and D),  $y$ - $z$  MIPs (Fig. 5, B and E), and volume-rendered images (Fig. 5, C and F). The volume-rendered images of the *Pkd1<sup>wt/wt</sup>* (Fig. 5C) and *Pkd1<sup>nl/nl</sup>* (Fig. 5F) kidneys were manually segmented to exclude any signals from the adjacent spleen and superficial skin vasculature. From these images, it can be seen that the ordered vessel tree characteristic of the wild-type kidney is not present

in the PKD case. This can be observed most clearly in the  $y$ - $z$  MIPs and the volume-rendered images, particularly the animated representations of the latter (Supplemental Movies S6 and S7). Instead of the ordered branching structure of the vasculature in *Pkd1<sup>wt/wt</sup>* kidneys, the *Pkd1<sup>nl/nl</sup>* mouse has a disorganized and chaotic network of renal vessels, which is consistent with the ex vivo images in Fig. 4.

Our previous work using immunohistochemistry for a pan-endothelial marker, platelet/endothelial cell adhesion molecule 1 (CD31), demonstrated subtle changes in the renal microvasculature of *Pkd1<sup>nl/nl</sup>* mice early in disease progression (12). To determine whether PAI could also detect early alterations in the vascular anatomy of *Pkd1<sup>nl/nl</sup>* mice, we imaged 8-day-old *Pkd1<sup>wt/wt</sup>* and *Pkd1<sup>nl/nl</sup>* mice. PA images acquired in vivo are shown in Fig. 6 as volume-rendered images with the kidneys manually segmented and false colored; the animated representations of these images (Supplemental Movies S8 and S9) reveal the renal vasculature most clearly. Horizontal (Fig. 6, A and B) and transverse (Fig. 6, C and D) viewpoints for *Pkd1<sup>wt/wt</sup>* and *Pkd1<sup>nl/nl</sup>* are shown. Visual inspection of these images suggests that the renal vasculature of the *Pkd1<sup>nl/nl</sup>* mice is characterized by reduced vessel density, vascular dilation, and increased disorder compared with the *Pkd1<sup>wt/wt</sup>* case. The

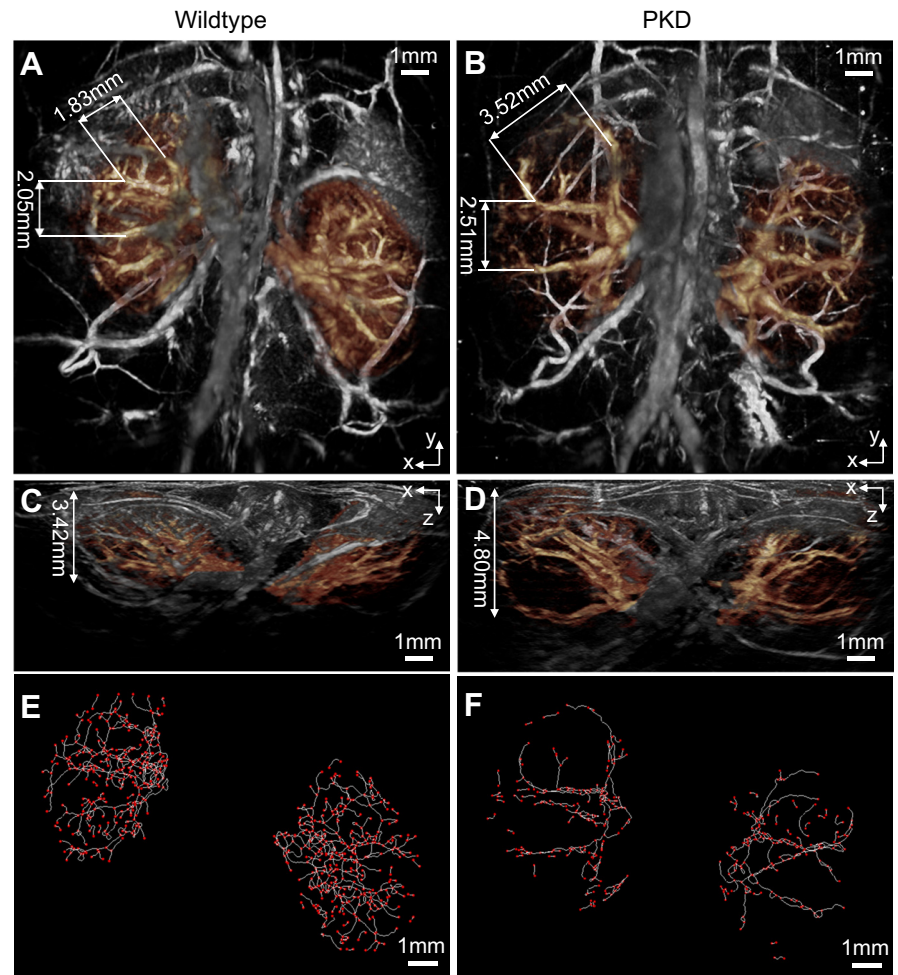
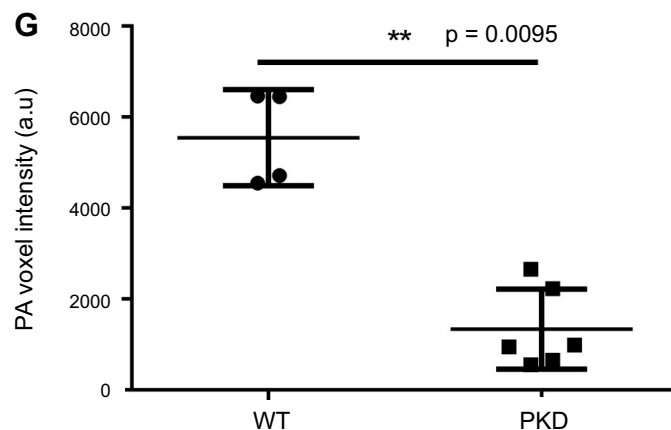


Fig. 6. In vivo volume-rendered PA images of the abdominal cavity of an 8-day-old *Pkd1*<sup>wt/wt</sup> (A and C) and *Pkd1*<sup>nl/nl</sup> (B and D) mouse. An animated representation of the images can be viewed online at Supplemental Movies S8 and S9. The viewpoints in A and B are horizontal (x-y), while C and D are vertical (x-z) views of 3D data sets acquired at an excitation wavelength of 850 nm. The kidneys have been manually segmented and false colored. The separation between similar renal vessels in the wild-type and PKD mouse is larger in the PKD mouse, consistent with the PKD kidney being larger than the wild type. Skeleton of the network of vessels extracted from the PA images for wild-type (E) and PKD (F) mouse kidneys. The total number of branching nodes (red dots) is 619 in the wild-type kidneys, compared with 372 in the PKD. There are 699 vessel segments (white lines between nodes) in the wild-type kidneys compared 409 in the PKD. The number of vessel segments and branches in the PKD are ~60% of those in the wild-type kidneys. G: mean PA voxel signal intensities obtained in ( $n = 4$ ) wild-type kidneys and ( $n = 6$ ) PKD kidneys. The mean value for the wild type is 5,546 with a SD of 1,055, while the mean for the PKD kidneys is 1,339 and the SD is 880. A two tailed Mann-Whitney test shows a statistically significant difference ( $P = 0.0095$ ) between the groups.



latter is most apparent in the animated movies that show that the *Pkd1*<sup>nl/nl</sup> renal vascular architecture bears little resemblance to the characteristic hierarchical tree-like structure of the normal kidney vasculature. To provide a more quantitative comparison of the structure of the vasculature, we first measured the separation distance between specific corresponding vessels in a *Pkd1*<sup>wt/wt</sup> and *Pkd1*<sup>nl/nl</sup> kidney. We found that this parameter was increased in the *Pkd1*<sup>nl/nl</sup> mouse compared with the

*Pkd1*<sup>wt/wt</sup> as indicated in Fig. 6, A and B. For example, the separation between two specific renal vessels is 2.05 mm in the *Pkd1*<sup>wt/wt</sup> kidney, while the separation between the same pair of vessels in *Pkd1*<sup>nl/nl</sup> mice is 2.51 mm. A second pair of vessels shows a separation of 1.83 mm for the wild-type kidney and 3.52 mm for PKD. Second, we undertook a statistical analysis of ( $n = 8$ ) vessels, and this showed a mean vessel diameter of 0.25 mm, with a standard deviation of 0.05 mm in

the wild-type kidneys. In the PKD kidneys, the mean diameter of the vessels is 0.34 mm with a standard deviation of 0.1 mm suggesting the vessels are dilated. Moreover, even at this early stage of the disease progression, the renal vasculature in the *Pkd1<sup>nl/nl</sup>* mouse appears more sparsely distributed than that of the normal *Pkd1<sup>wt/wt</sup>* mouse. This is most apparent in the skeletons of the renal vascular network extracted from the PA images (Fig. 6, *E* and *F*). The total number of branching points (red dots) in the *Pkd1<sup>wt/wt</sup>* kidneys (Fig. 6*E*) is nearly twofold higher than in the in the *Pkd1<sup>nl/nl</sup>* (Fig. 6*F*); 619 and 372, respectively. A similar pattern was observed in vessel segments (white lines between branch points) in the *Pkd1<sup>wt/wt</sup>* kidneys, compared with in *Pkd1<sup>nl/nl</sup>* kidneys (699 and 409 vessel segments, respectively).

The quantifications above are based on analysis of only those vessels in the renal vasculature that can be spatially resolved by the scanner. However, smaller vessels (e.g., capillaries) that cannot be individually resolved still provide detectable spatially averaged PA contrast which is representative of the renal vasculature. Therefore, a metric that represents both resolvable and subresolution vasculature is also desirable. To this end, the mean intensities of voxels above the noise floor for each segmented kidney were obtained (Fig. 6*G*) for both *Pkd1<sup>wt/wt</sup>* ( $n = 4$  kidneys from 2 individual animals) and *Pkd1<sup>nl/nl</sup>* ( $n = 6$  kidneys from 3 individual animals). The noise floor was obtained by estimating the standard deviation of voxels in a data set acquired on the PA scanner without a mouse present and multiplying by a factor of three to provide the peak value. The mean intensity from the *Pkd1<sup>wt/wt</sup>* kidneys is 5,546 with a standard deviation of 1055. This value is approximately four times higher than the mean of 1,339 obtained from the *Pkd1<sup>nl/nl</sup>* with a standard deviation of 880. A two tailed Mann-Whitney test shows a statistically significant difference ( $P = 0.0095$ ) between the groups. The higher voxel intensities in the wild type is consistent with a greater vascular density in the wild-type kidneys compared with the PKD.

## DISCUSSION

**Conclusion.** This study has demonstrated the use of PAI to acquire noninvasive, label-free, 3D in vivo images of the murine kidney and its vasculature, with anatomical structures such as the spine, ribs, and spleen also visible. The level of structural detail of the kidney visualized in this study is unprecedented for PAI, with individual renal blood vessels and their branching visible. To achieve these results, a high-resolution 3D PA scanner based on an all optical ultrasound sensor was used. Its broad detection bandwidth, small element size, and high sensitivity result in significant improvements in image quality, compared with previous PA renal imaging studies that have used conventional piezoelectric detector-based scanners. The depth-dependent spatial resolution of the PA images obtained in this study, which lie within the range of 59–158  $\mu\text{m}$ , is comparable to that achievable with MRI and ultrasound, but unlike these modalities there is no requirement for exogenous contrast agents to visualize the microvasculature due to the strong intrinsic PA contrast provided by hemoglobin. The spatial resolution is not quite as high as the 35- $\mu\text{m}$  resolution obtained in vivo with micro-CT for studying the microvasculature in mouse models of ischemia-reperfusion, unilateral ureteral obstruction, and Alport syndrome (10). However,

unlike micro-CT, PAI does not require contrast agents or employ ionising radiation, which enables vascular changes to be monitored longitudinally with an unlimited number of image acquisitions. Moreover, although the current study has focused on the use of PAI to visualize renal vascular anatomy, the technique also has the potential to provide physiological parameters such as blood oxygen saturation (1, 7) and blood flow velocity (4) simultaneously, which is not possible with existing imaging modalities. Blood oxygenation saturation can, in principle, be determined by acquiring PA images at multiple wavelengths and applying a spectroscopic inversion to estimate the concentrations of oxy and deoxyhemoglobin (7). Blood flow velocity measurements exploit the PA Doppler effect, and has been demonstrated in phantoms (4) and superficial vessels such as those in the mouse ear (33). Although both methods still require further development for use at the depths relevant to the current study, they offer the prospect of further increasing the utility of PAI for the study of renal disease. For example, it has been hypothesized that hypoxia is an important triggering stimuli, which precedes vascular dysfunction in CKDs (21), and PA functional imaging could help study the relevant oxygen supply and delivery distribution.

To explore the feasibility of using PAI to study renal diseases, a preliminary study in which a mouse model of autosomal dominant PKD was imaged at early (8 days) and late stages (12 wk) of the disease was undertaken. Prior studies in patients and mouse models using corrosion casting, angiography, and immunohistochemistry have shown that the architecture of the renal vasculature is disrupted in autosomal dominant PKD, with the appearance of tortuous, abnormally patterned and dilated vessels surrounding cyst epithelia (2, 30). The PA images of *Pkd1<sup>nl/nl</sup>* mice are broadly consistent with these findings. At 12 wk of age, the images revealed that the structured vessel branching pattern in healthy wild-type kidneys is replaced with a more disorganized distribution in PKD. In addition, the number of vessels was observed to be reduced in PKD, compared with the wild type. The disorganized vessel structure and reduction in vascular density were also observed at the early disease stage. At 8 days of age, when small cysts are observed (12), the numbers of vessel segments and branching points in the PKD kidneys were ~60% of those in the age-matched wild-type kidneys. These results are broadly consistent with previously published data (32), from ex vivo micro-CT studies which have shown that the total vascular density in PKD rats is 50% less than in the wild-type case. Interestingly, our prior studies have shown an increase in the CD31<sup>+</sup> noncystic area in *Pkd1<sup>nl/nl</sup>* mice from 1 day of age (12). However, since we found that active angiogenesis does not occur at this time point (based on colocalization of CD31 and the proliferation marker Ki67), this may be due to vessels becoming dilated and occupying a greater surface area. This too is broadly consistent with the PAI data that suggests that there are fewer vessels in *Pkd1<sup>nl/nl</sup>* mice but they are dilated. In addition to changes in vessels that can be clearly resolved, the PAI data also showed that the subresolution vasculature, which provides spatially averaged PA contrast, also provides physiologically relevant information. An analysis of the signal intensities of all voxels above the noise floor revealed that the mean voxel intensity of the *Pkd1<sup>wt/wt</sup>* mice is significantly higher than the *Pkd1<sup>nl/nl</sup>* animals by approximately a factor of four. Although additional more extensive studies, including

side-by-side comparison with other imaging modalities such as micro-CT, are required to fully establish the utility of PAI in this context, these preliminary results suggest it could be a useful tool for studying vascular changes implicated in PKD.

Currently, in vivo imaging techniques such as MRI and ultrasound are utilized in the study of PKD to monitor cystogenesis and measure the increase in total kidney volume (11) (9). The use of noninvasive PAI to monitor renal vascular changes due to PKD could complement these measurements since the renal vasculature has been implicated in playing a role in cyst formation, as well as other etiologies of CKD (21). As part of future work, disease staging could be achieved by longitudinally monitoring the renal vasculature changes in transgenic mouse models of PKD and correlating the severity of vascular malformations as the disease progresses with age. In addition, the efficacy of therapeutic interventions, such as vascular endothelial growth factor C administration, which partly work by normalizing the defective vasculature in PKD (12), could also be studied longitudinally. Allied to these disease-staging and therapy-monitoring studies would be the development of additional quantitative methods of vascular analysis, for example, measurements of vessel diameter, branching, and tortuosity, which have been shown to change in progressive kidney diseases (10).

In summary, this study suggests that PAI could be a useful and versatile preclinical tool for characterizing the progression of kidney disease in mouse models, particularly in circumstances where a relatively low-cost, label-free functional imaging modality that does not use ionizing radiation is required.

#### ACKNOWLEDGMENTS

We thank Dorien Peters (Dept. of Human Genetics, Leiden, The Netherlands) for the provision of *Pkd1<sup>nl/nl</sup>* mice.

#### GRANTS

J. J. Connell is funded by the UK Regenerative Medicine Platform. D. A. Long and J. L. Huang acknowledge support from a project grant from Kidney Research UK (RP38/2013) and the National Institute for Health Research Biomedical Research Centre at Great Ormond Street Hospital for Children National Health Service Foundation Trust and University College London. M. F. Lythgoe receives funding from the Medical Research Council (MR/J013110/1); the National Centre for the Replacement, Reduction and Refinement of Animal in Research (NC3Rs); UK Regenerative Medicine Platform Safety Hub (MRC: MR/K026739/1); Eli Lilly and Company. This work was supported by King's College London and University College London Comprehensive Cancer Imaging Centre, Cancer Research UK and the Engineering and Physical Sciences Research Council, in association with the Medical Research Council and Department of Health, UK, and European Union project FAMOS (FP7 ICT, Contract 317744).

#### DISCLOSURES

No conflicts of interest, financial or otherwise, are declared by the authors.

#### AUTHOR CONTRIBUTIONS

O.O., J.J.C., J.L.H., M.F.L., D.A.L., and P.B. conceived and designed research; O.O., J.J.C., J.L.H., and E.Z. performed experiments; O.O., J.J.C., and J.L.H. analyzed data; O.O., J.J.C., D.A.L., and P.B. interpreted results of experiments; O.O. and J.J.C. prepared figures; O.O. and J.J.C. drafted manuscript; O.O., J.J.C., M.F.L., D.A.L., and P.B. edited and revised manuscript; O.O., J.J.C., J.L.H., E.Z., M.F.L., D.A.L., and P.B. approved final version of manuscript.

#### REFERENCES

1. Beard P. Biomedical photoacoustic imaging. *Interface Focus* 1: 602–631, 2011. doi:10.1098/rsfs.2011.0028.
2. Bello-Reuss E, Holubec K, Rajaraman S. Angiogenesis in autosomal-dominant polycystic kidney disease. *Kidney Int* 60: 37–45, 2001. doi:10.1046/j.1523-1755.2001.00768.x.
3. Brecht HP, Su R, Fronheiser M, Ermilov SA, Conjusteau A, Oraevsky AA. Whole-body three-dimensional optoacoustic tomography system for small animals. *J Biomed Opt* 14: 064007, 2009. doi:10.1117/1.3259361.
4. Brunker J, Beard P. Velocity measurements in whole blood using acoustic resolution photoacoustic Doppler. *Biomed Opt Express* 7: 2789–2806, 2016. doi:10.1364/BOE.7.002789.
5. Buehler A, Herzog E, Razansky D, Ntziachristos V. Video rate optoacoustic tomography of mouse kidney perfusion. *Opt Lett* 35: 2475–2477, 2010. doi:10.1364/OL.35.002475.
6. Chade AR, Tullios NA, Harvey TW, Mahdi F, Bidwell GL 3rd. Renal therapeutic angiogenesis using a bioengineered polymer-stabilized vascular endothelial growth factor construct. *J Am Soc Nephrol* 27: 1741–1752, 2016. doi:10.1681/ASN.2015040346.
7. Cox B, Laufer JG, Arridge SR, Beard PC. Quantitative spectroscopic photoacoustic imaging: a review. *J Biomed Opt* 17: 061202, 2012. doi:10.1117/1.JBO.17.6.061202.
8. Dessapt-Baradez C, Woolf AS, White KE, Pan J, Huang JL, Hayward AA, Price KL, Kolatsi-Joannou M, Locatelli M, Diennet M, Webster Z, Smillie SJ, Nair V, Kretzler M, Cohen CD, Long DA, Gnudi L. Targeted glomerular angiopoietin-1 therapy for early diabetic kidney disease. *J Am Soc Nephrol* 25: 33–42, 2014. doi:10.1681/ASN.2012121218.
9. Spithoven EM, van Gastel MD, Messchendorp AL, Casteleijn NF, Drenth JP, Gaillard CA, de Fijter JW, Meijer E, Peters DJ, Kappert P, Renken RJ, Visser FW, Wetzels JF, Zietse R, Gansevoort RT, d'Agnolo H, Casteleijn NF, Dekker H, Drenth J, de Fijter JW, Gansevoort RT, Gevers TJ, Happé H, ter Horst G, Kappert P, Meijer E, Peters DJM, Renken R, Pieterman H, Salihi M, Soonawala D, Spithoven EM, Torres VE, Wasser M, Wetzels JFM, Zietse R, Drenth J, de Fijter JW, Gansevoort RT, Meijer E, Peters DJM, Torres VE, Wetzels JF, Zietse R, Gaillard CA, van Buren M, Veeger N, Vervloet M; DIPAK Consortium. Estimation of total kidney volume in autosomal dominant polycystic kidney disease. *Am J Kidney Dis* 66: 792–801, 2015. doi:10.1053/j.ajkd.2015.06.017.
10. Ehling J, Bábíčková J, Gremse F, Klinkhammer BM, Baetke S, Kneuchel R, Kiessling F, Floege J, Lammers T, Boor P. Quantitative micro-computed tomography imaging of vascular dysfunction in progressive kidney diseases. *J Am Soc Nephrol* 27: 520–532, 2016. doi:10.1681/ASN.2015020204.
11. Grantham JJ, Torres VE. The importance of total kidney volume in evaluating progression of polycystic kidney disease. *Nat Rev Nephrol* 12: 667–677, 2016. doi:10.1038/nrneph.2016.135.
12. Huang JL, Woolf AS, Kolatsi-Joannou M, Baluk P, Sandford RN, Peters DJM, McDonald DM, Price KL, Winyard PJD, Long DA. Vascular endothelial growth factor c for polycystic kidney diseases. *J Am Soc Nephrol* 27: 69–77, 2016. doi:10.1681/ASN.2014090856.
13. Jathoul AP, Laufer J, Ogunlade O, Treeby B, Cox B, Zhang E, Johnson P, Pizzey AR, Philip B, Marafioti T, Lythgoe MF, Pedley RB, Pule MA, Beard P. Deep in vivo photoacoustic imaging of mammalian tissues using a tyrosinase-based genetic reporter. *Nat Photonics* 9: 239–246, 2015. doi:10.1038/nphoton.2015.22.
14. Kobayashi H, Kawamoto S, Jo S-K, Sato N, Saga T, Hiraga A, Konishi J, Hu S, Togashi K, Brechbiel MW, Star RA. Renal tubular damage detected by dynamic micro-MRI with a dendrimer-based magnetic resonance contrast agent. *Kidney Int* 61: 1980–1985, 2002. doi:10.1046/j.1523-1755.2002.00364.x.
15. Lam RB, Kruger RA, Reinecke DR, DelRio SP, Thornton MM, Picot PA, Morgan TG. Dynamic optical angiography of mouse anatomy using radial projections. *Proc SPIE* 7564: 1–7, 2010. doi:10.1117/12.841024.
16. Lantinga-van Leeuwen IS, Dauwse JG, Baelde HJ, Leonhard WN, van de Wal A, Ward CJ, Verbeek S, Deruiter MC, Breuning MH, de Heer E, Peters DJ. Lowering of *Pkd1* expression is sufficient to cause polycystic kidney disease. *Hum Mol Genet* 13: 3069–3077, 2004. doi:10.1093/hmg/ddh336.
17. Laufer J, Johnson P, Zhang E, Treeby B, Cox B, Pedley B, Beard P. In vivo preclinical photoacoustic imaging of tumor vasculature development and therapy. *J Biomed Opt* 17: 056016, 2012. doi:10.1117/1.JBO.17.5.056016.
18. Laufer J, Norris F, Cleary J, Zhang E, Treeby B, Cox B, Johnson P, Scambler P, Lythgoe M, Beard P. In vivo photoacoustic imaging of mouse embryos. *J Biomed Opt* 17: 061220, 2012. doi:10.1117/1.JBO.17.6.061220.

19. Lindner JR, Song J, Christiansen J, Klibanov AL, Xu F, Ley K. Ultrasound assessment of inflammation and renal tissue injury with microbubbles targeted to P-selectin. *Circulation* 104: 2107–2112, 2001. doi:10.1161/hc4201.097061.
20. Liu B, Gattone VH 2nd, Kruger RA, Stantz KM. Assessment of photoacoustic computed tomography to classify tissue in a polycystic-kidney disease mouse model. *Proc SPIE* 6086: 1–8, 2006. doi:10.1117/12.646180.
21. Long DA, Norman JT, Fine LG. Restoring the renal microvasculature to treat chronic kidney disease. *Nat Rev Nephrol* 8: 244–250, 2012. doi:10.1038/nrneph.2011.219.
22. Pang P, Abbott M, Chang SL, Abdi M, Chauhan N, Mistri M, Ghofrani J, Fucci QA, Walker C, Leonardi C, Grady S, Halim A, Hoffman R, Lu T, Cao H, Tullius SG, Malek S, Kumar S, Steele G, Kibel A, Freedman BS, Waikar SS, Siedlecki AM. Human vascular progenitor cells derived from renal arteries are endothelial-like and assist in the repair of injured renal capillary networks. *Kidney Int* 91: 129–143, 2017. doi:10.1016/j.kint.2016.07.037.
23. Scarfe L, Rak-Raszewska A, Geraci S, Darssan D, Sharkey J, Huang J, Burton NC, Mason D, Ranjzad P, Kenny S, Gretz N, Lévy R, Kevin Park B, García-Fiñana M, Woolf AS, Murray P, Wilm B. Measures of kidney function by minimally invasive techniques correlate with histological glomerular damage in SCID mice with adriamycin-induced nephropathy. *Sci Rep* 5: 13601, 2015. doi:10.1038/srep13601.
24. Singh J, Daftary A. Iodinated contrast media and their adverse reactions. *J Nucl Med Technol* 36: 69–74, 2008. doi:10.2967/jnmt.107.047621.
25. Song KH, Wang LV. Noninvasive photoacoustic imaging of the thoracic cavity and the kidney in small and large animals. *Med Phys* 35: 4524–4529, 2008. doi:10.1118/1.2977534.
26. Treeby BE. Acoustic attenuation compensation in photoacoustic tomography using time-variant filtering. *J Biomed Opt* 18: 036008, 2013. doi:10.1117/1.JBO.18.3.036008.
27. Treeby BE, Cox BT. k-Wave: MATLAB toolbox for the simulation and reconstruction of photoacoustic wave fields. *J Biomed Opt* 15: 021314, 2010. doi:10.1117/1.3360308.
28. Treeby BE, Varslot TK, Zhang EZ, Laufer JG, Beard PC. Automatic sound speed selection in photoacoustic image reconstruction using an autofocus approach. *J Biomed Opt* 16: 090501, 2011. doi:10.1117/1.3619139.
29. Treeby BE, Zhang EZ, Cox BT. Photoacoustic tomography in absorbing acoustic media using time reversal. *Inverse Probl* 26: 115003, 2010. doi:10.1088/0266-5611/26/11/115003.
30. Wei W, Popov V, Walocha JA, Wen J, Bello-Reuss E. Evidence of angiogenesis and microvascular regression in autosomal-dominant polycystic kidney disease kidneys: a corrosion cast study. *Kidney Int* 70: 1261–1268, 2006. doi:10.1038/sj.ki.5001725.
31. Wolfensohn S, Lloyd M. *Handbook of Laboratory Animal Management and Welfare*. Hoboken, NJ: Wiley, 2008.
32. Xu R, Franchi F, Miller B, Crane JA, Peterson KM, Psaltis PJ, Harris PC, Lerman LO, Rodriguez-Porcel M. Polycystic kidneys have decreased vascular density: a micro-CT study. *Microcirculation* 20: 183–189, 2013. doi:10.1111/micc.12022.
33. Yao J, Maslov KI, Shi Y, Taber LA, Wang LV. In vivo photoacoustic imaging of transverse blood flow by using Doppler broadening of bandwidth. *Opt Lett* 35: 1419–1421, 2010. doi:10.1364/OL.35.001419.
34. Yasuda K, Park HC, Ratliff B, Addabbo F, Hatzopoulos AK, Chander P, Goligorsky MS. Adriamycin nephropathy: a failure of endothelial progenitor cell-induced repair. *Am J Pathol* 176: 1685–1695, 2010. doi:10.2353/ajpath.2010.091071.
35. Zhang E, Laufer J, Beard P. Backward-mode multiwavelength photoacoustic scanner using a planar Fabry-Perot polymer film ultrasound sensor for high-resolution three-dimensional imaging of biological tissues. *Appl Opt* 47: 561–577, 2008. doi:10.1364/AO.47.000561.

